Sustainable Cities and Society 96 (2023) 104682

Contents lists available at ScienceDirect

Sustainable Cities and Society

journal homepage: www.elsevier.com/locate/scs

A suction method to mitigate pressure waves induced by high-speed maglev trains passing through tunnels

Zheng-Wei Chen [a,b,†], Zhan-Hao Guo [a,b,†], Yi-Qing Ni [a,b,*], Tang-Hong Liu [c,d,e,f], Jie Zhang [c,d,e,f]

[a] National Rail Transit Electrification and Automation Engineering Technology Research Center (Hong Kong Branch), Hong Kong, China
[b] Department of Civil and Environmental Engineering, The Hong Kong Polytechnic University, Hong Kong, China
[c] The State Key Laboratory of Heavy-duty and Express High-power Electric Locomotive, Central South University, Changsha 410075, China
[d] Key Laboratory of Traffic Safety on Track of Ministry of Education, School of Traffic & Transportation Engineering, Central South University, Changsha 410075, China
[e] National & Local Joint Engineering Research Center of Safety Technology for Rail Vehicle, Central South University, Changsha 410075, China
[f] Key Laboratory of Railway Industry of Aerodynamics, Central South University, Changsha 410075, China

ARTICLE INFO

Keywords:
High-speed maglev train
Tunnel
Micro-pressure wave
Suction method
Sustainable cities

ABSTRACT

When a high-speed maglev train travels through a tunnel, sudden pressure changes are generated in the tunnel, which have a negative impact on the comfort of passengers and the service life of equipment. Moreover, a strong micro-pressure wave is radiated, causing environmental noise at the tunnel exit. Using the unsteady compressible Reynolds-averaged Navier–Stokes equations based on the shear stress transport k-ω turbulence model, this study investigates the effectiveness of suction (deployed on the tunnel wall) to mitigate the pressure waves and compares the results obtained under different suction velocities. The results show that when the suction is actuated, a low-pressure region is generated near the suction slots, which can trim down the initial compression wave and the high-pressure region in front of the train. Moreover, the instantaneous train surface pressure, tunnel surface pressure and micro-pressure wave have a significant relationship with the suction velocity. For instance, compared to the no suction case, the suction-actuated case with the suction velocity of 50 m/s contributes to an amplitude reduction of 10.44% and 30.61% for the first and second sudden pressure changes, respectively, at train surface measuring point H1 (at the nose of the train); an amplitude reduction of more than 14% for the sudden pressure change at tunnel surface measuring point T17 (at the middle of the tunnel); and an amplitude reduction of 12.44% for the micro-pressure wave at measuring point M2 (outside the tunnel and 20 m from the tunnel exit). These indicate that the suction technique can be employed to alleviate the tunnel aerodynamic effect. Also, the results obtained under different suction velocities can serve as a guide for the design of suction actuators.

1. Introduction

Railway transportation is a vital sustainable system connecting passengers and goods across the world due to its ecological nature and immense capacity (Lin et al., 2021; Schmutzler, 2021). Despite this, railway transportation faces many challenges and opportunities. For instance, the limited accessibility and flexibility of railway transportation make it difficult to offer the first and last mile travel for passengers and goods. Meanwhile, the development of new transportation technologies is providing more efficient solutions to these challenges, such as bike sharing systems (Guo et al., 2021; Yu et al., 2021), drone transport systems (Kellermann et al., 2020; Zailani et al., 2020), and intelligent transport systems (Chehri & Mouftah, 2019; Dogaroglu et al., 2021). On the other hand, limited by the friction force, the development of contact-type rail has gradually reached a bottleneck (Fang et al., 2018). Thus, the maglev train has become the main research focus of new generation of high-speed transport systems, benefiting from its advantages of faster speed, lower energy consumption, higher stability, and less impact on the environment (Sun et al., 2021).

In recent decades, the operating speed of maglev trains has made a great breakthrough. The Shanghai high-speed maglev reached the maximum commercial operating speed of 430 km/h (Shi et al., 2022; Vuchic & Casello, 2002). The L0 Series maglev in Japan set a world record of the ultrahigh speed at 603 km/h in 2015 (Dong et al., 2019; Han & Kim, 2016). The 600 km/h high-speed maglev was rolled out in

* Corresponding author.
E-mail address: ceyqni@polyu.edu.hk (Y.-Q. Ni).
† These authors contributed equally to this work.

https://doi.org/10.1016/j.scs.2023.104682
Received 17 January 2023; Received in revised form 21 April 2023; Accepted 27 May 2023
Available online 29 May 2023

Nomenclature

C_{H1}	Initial compression wave generated by the head car entering the tunnel
C_{H3}	Third-reflected compression wave generated by the reflection of the second-reflected expansion wave
C_{T2}	Second-reflected compression wave generated by the reflection of initial expansion wave
E_{H2}	Second-reflected expansion wave generated by the reflection of initial compression wave
E_{T1}	Initial expansion wave generated by the tail car entering the tunnel
E_{T3}	Third-reflected expansion wave generated by the reflection of the second-reflected compression wave
H1-H33	Maglev train surface pressure measuring points
H_{tr}	Height of the maglev train
k	Turbulence kinetic energy
L_{tr}	Length of the maglev train
L_{tu}	Length of the tunnel
M1-M10	Micro-pressure wave measuring points
S_{tu}	Cross-sectional area of the tunnel
SV10	Suction velocity at 10 m/s
SV20	Suction velocity at 20 m/s
SV30	Suction velocity at 30 m/s
SV40	Suction velocity at 40 m/s
SV50	Suction velocity at 50 m/s
t	Time
T1-T31	Tunnel surface pressure measuring points
USV	Unactuated suction velocity case
w	Specific dissipation rate
W_{tr}	width of the maglev train

Abbreviations

CFD	Computational fluid dynamics
FSPC	First sudden pressure change
ICW	Initial compression wave
MPW	Micro-pressure wave
MPWs	Micro-pressure waves
SSPC	Second sudden pressure change
SST	Shear stress transport
TSPC	Third sudden pressure change

China (Lin & Sheng, 2018; Schmid et al., 2021). However, the state-of-the-art maglev technology has not completely resolved the potential environmental and riding comfort issues associated with the running speed from 400 km/h to 600 km/h (Han & Kim, 2018; Minelli et al., 2021; Zhou et al., 2021). One of the critical challenges resides in the generation of compression waves, expansion waves, and micro-pressure waves (MPWs) when a high-speed maglev train passes through tunnels (Han et al., 2022; Zhou et al., 2022) as shown in Fig. 1. These waves can cause significant pressure disturbances in the tunnel, leading to noise and other aerodynamic issues. Thus, minimizing the impact of these waves is crucial for ensuring safe, efficient, and suitable operation of maglev trains in tunnels.

2. Literature review

The typical and efficient measures to resolve the above problem are the deployment of tunnel hoods and ventilation shafts (Li et al., 2022b; Saito et al., 2013; Xiang et al., 2018). In recent years, there are many studies addressing tunnel hoods, including the investigations on oblique hoods (Zhang et al., 2017, 2018), enlarged section hoods (Li et al., 2019;

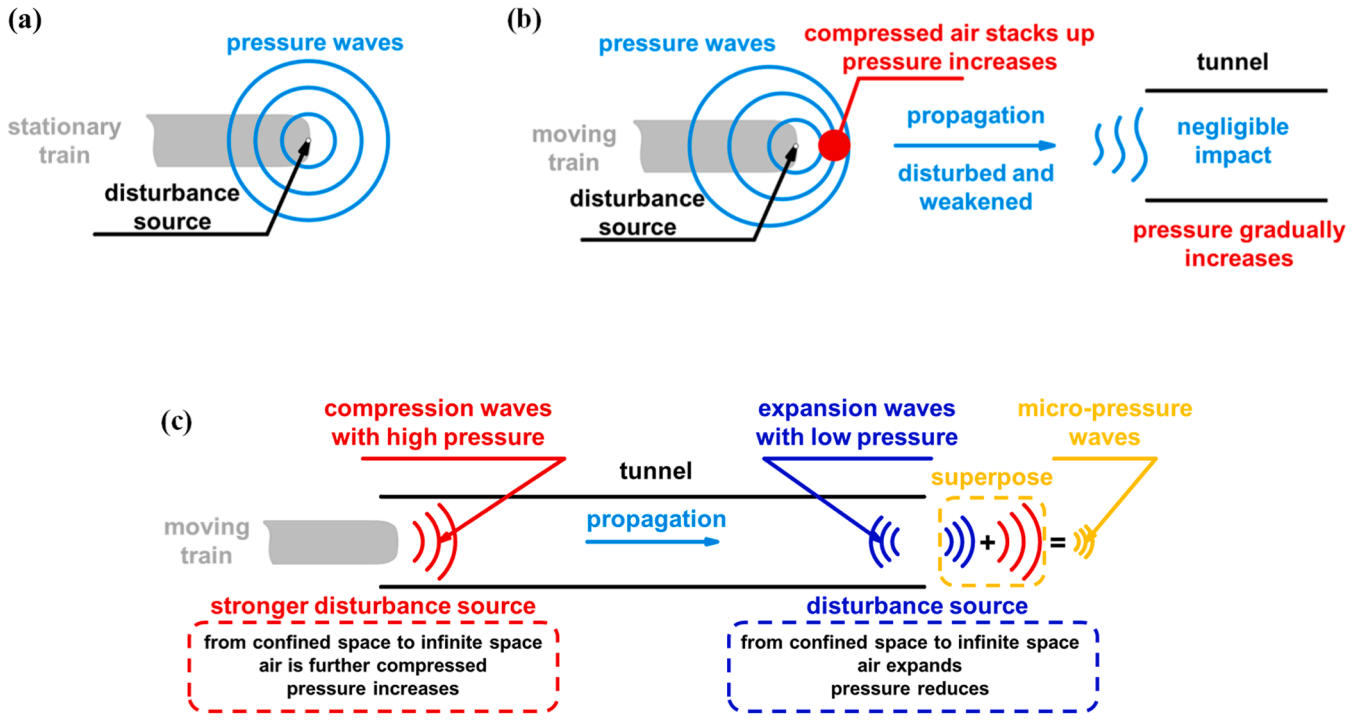

Fig. 1. (a) Generation of pressure waves by a stationary train; (b) generation of pressure waves by a moving train; (c) generation of compression waves, expansion waves, and micro-pressure waves in the train/tunnel aerodynamics. (For interpretation of the references to color in this figure legend, the reader is referred to the web version of this article.)

Wang et al., 2018) or windows on tunnel hoods (Miyachi & Fukuda, 2021; Okubo et al., 2022). Apart from the traditional tunnel hoods, a bio-mimic tunnel hood has been developed by imitating the respiration of hunter shark gills (Kim et al., 2021a, 2021b). Like the research made on tunnel hoods, the majority of studies on ventilation shafts have focused on parametric investigations, including the location, ratio and shape of ventilation shafts (Luo et al., 2020; Xiang et al., 2018). Only passive approaches were addressed in the previous studies where different tunnel hoods and ventilation shafts require different tunnel external or internal structures, respectively. While a ventilation hood or ventilation shaft can be well designed in advance, their alleviation effect may be insufficient as the running speed of train increases. Furthermore, due to the complex environment around a tunnel, it is oftentimes difficult to construct a ventilation hood or ventilation shaft in practice. Compared with the passive mitigation methods, active mitigation methods are more flexible and competitive.

Inspired by vacuum cube high-speed trains (Gillani et al., 2019; Zhong et al., 2021), tunnel ventilation technology (Li & Chen, 2019; Zhang & Li, 2021) and active flow control techniques used in high-speed trains and large-scale bridges (Chen et al., 2022; Xue et al., 2021), this study explores the feasibility of active suction on tunnel walls to mitigate pressure variations in tunnels, thereby further alleviating the interaction of maglev train/tunnel aerodynamics. The novelty of this study and its potential contribution to healthy transportation and resilient environments are summarized as follows:

- The flow topologies, train surface pressure, tunnel surface pressure, and micro-pressure wave with and without suction are compared in this study, with intent to investigate whether the suction control could affect the propagation of pressure waves, thereby providing insights into the behavior of suction actuation on the maglev train/tunnel aerodynamic effects.
- Building on the above study, the train surface pressure, tunnel surface pressure, and micro-pressure wave obtained under different suction velocities are comparatively analyzed in detail, to examine the influence of suction velocity on the propagation of pressure waves, which could serve as a guidance for tunnel engineers in designing and implementing the suction actuation to alleviate the maglev train/tunnel aerodynamic effects.

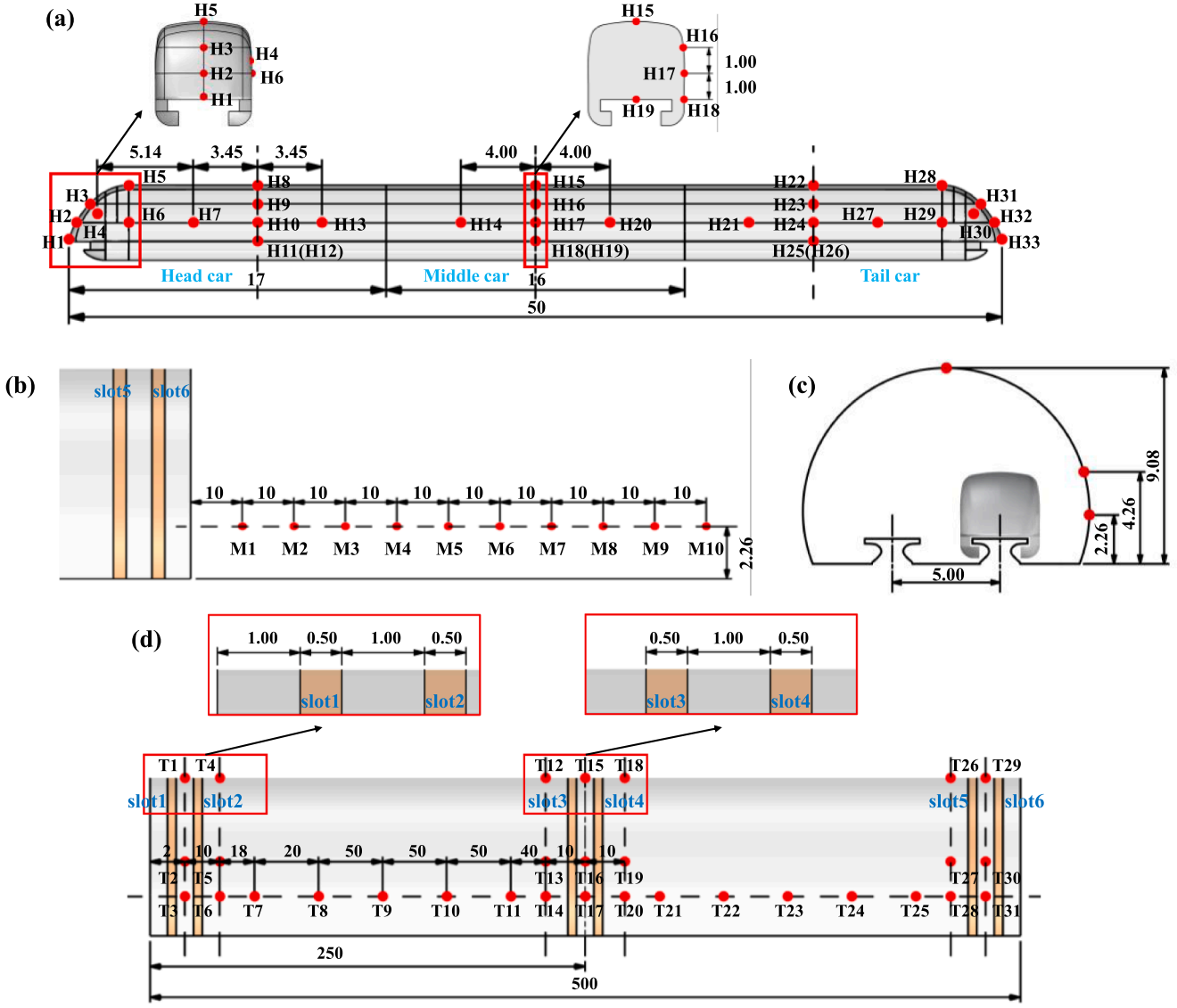

Fig. 2. Pressure measuring points and model: (a) train surface pressure measuring points, (b) MPW measuring points, (c) front view of tunnel measuring points, and (d) side view of suction slots and tunnel surface pressure measuring points. (Unit: meter). (For interpretation of the references to color in this figure legend, the reader is referred to the web version of this article.)

The remaining sections below are structured as follows. The computational model, settings in numerical method, and validation are presented in Section 2. Section 3 provides an analysis about the influence of suction velocity on the maglev train surface pressure, tunnel surface pressure and micro-pressure wave (MPW). Conclusions are drawn in Section 4.

3. Methodology

3.1. Geometry model and computational domain

In this study, a full-scale, simplified high-speed maglev train model is considered to evaluate the influence of suction on the tunnel aerodynamic effects. As shown in Fig. 2, the maglev train of concern consists of three cars, with a total length of $L_{tr} = 50.00$ m, height of $H_{tr} = 4.00$ m and width of $W_{tr} = 3.70$ m, and its running speed is assumed to be 430 km/h. A double-track tunnel is considered with a line spacing of 5 m, and the length of the tunnel is $L_{tu} = 500$ m with a cross-sectional area of $S_{tu} = 100$ m^2. The position and dimension of the suction actuators are described in Fig. 2(d). There are three pairs of actuation slots positioned near the tunnel entrance, middle and exit, in coincidence with the wave generation, propagation and emission processes, respectively. To assess the effectiveness of multiple suction slots, paired actuation slots with a width of 0.50 m are adopted to monitor the pressure variations between them, with a spacing of 1.00 m between each pair.

To evaluate the impact of suction on wave propagation, a series of measuring points are arranged. Fig. 2(a) illustrates the locations of the train surface's measuring points H1 to H33 (near the tunnel side). Among them, the measuring points H1 to H6 and H28 to H33 are positioned on the streamline zone. In addition, to evaluate the pressure distribution of the train in the vertical direction, the middle cross-sections of the cars are monitored, i.e., H8 to H12 on the head car, H15 to H19 on the middle car, and H22 to H26 on the tail car. To analyze the pressure distribution along the longitudinal direction, measuring points H7, H13, H14, H20, H21 and H27 are positioned at the train's half-height. Similarly, Fig. 2(c) and (d) show the positions of measuring points on the tunnel surface. To evaluate the variation of the tunnel surface pressure, particularly along its length, measuring points are set at the level of train's half height, including T3, T6, T7, T8, T9 and others. Extra measuring points are arranged near the actuation slots, e.g., T1 to T6, T12 to T20, and T26 to T31. In addition, there are 10 MPW measuring points outside the tunnel exit, as shown in Fig. 2(b).

Fig. 3 shows the computational domain and its main dimensions. The sizes of the tunnel entrance domain are the same as those of the exit domain, with a length of 600 m, a width of 120 m and a height of 60 m. There is an initial distance of 100 m in front of the train. As for the boundary conditions, the no-slip wall is applied on the train, tunnel, track, and ground (ground surfaces include surfaces EFGH, A'B'C'D', BDFH, B'D'F'H') as shown in Fig. 3(a). The sides and top of the tunnel entrance domain (surfaces ABEF, CDGH, ABCD, ACEG) are treated as the pressure inlet boundary condition, while those of the tunnel exit domain (surfaces A'B'E'F', C'D'G'H', E'F'G'H', A'C'E'G') are the pressure outlet boundary condition; The reference pressures on the pressure inlet and outlet boundary conditions are both presumed static pressure (0 Pa). A uniform, constant velocity profile is given at the actuation slots, which is normal to the tunnel surface. To study the impact of suction velocity on the tunnel aerodynamic effects, five different suction velocities of 10, 20, 30, 40 and 50 m/s are considered, denoted as SV10, SV20, SV30, SV40 and SV50, respectively. When the suction slots are unactuated (denoted as USV), the slot surfaces are defined as no-slip wall.

As illustrated in Fig. 3(b), the sliding mesh method, which has been widely used in studying tunnel aerodynamic effects (Chen et al., 2017; Li et al., 2021b; Meng et al., 2021), is employed in this study. The computational domain is divided into the sliding domain and the static domain. The train is included in the sliding domain, and the others are in the static domain. The moving velocity of the sliding domain is set as

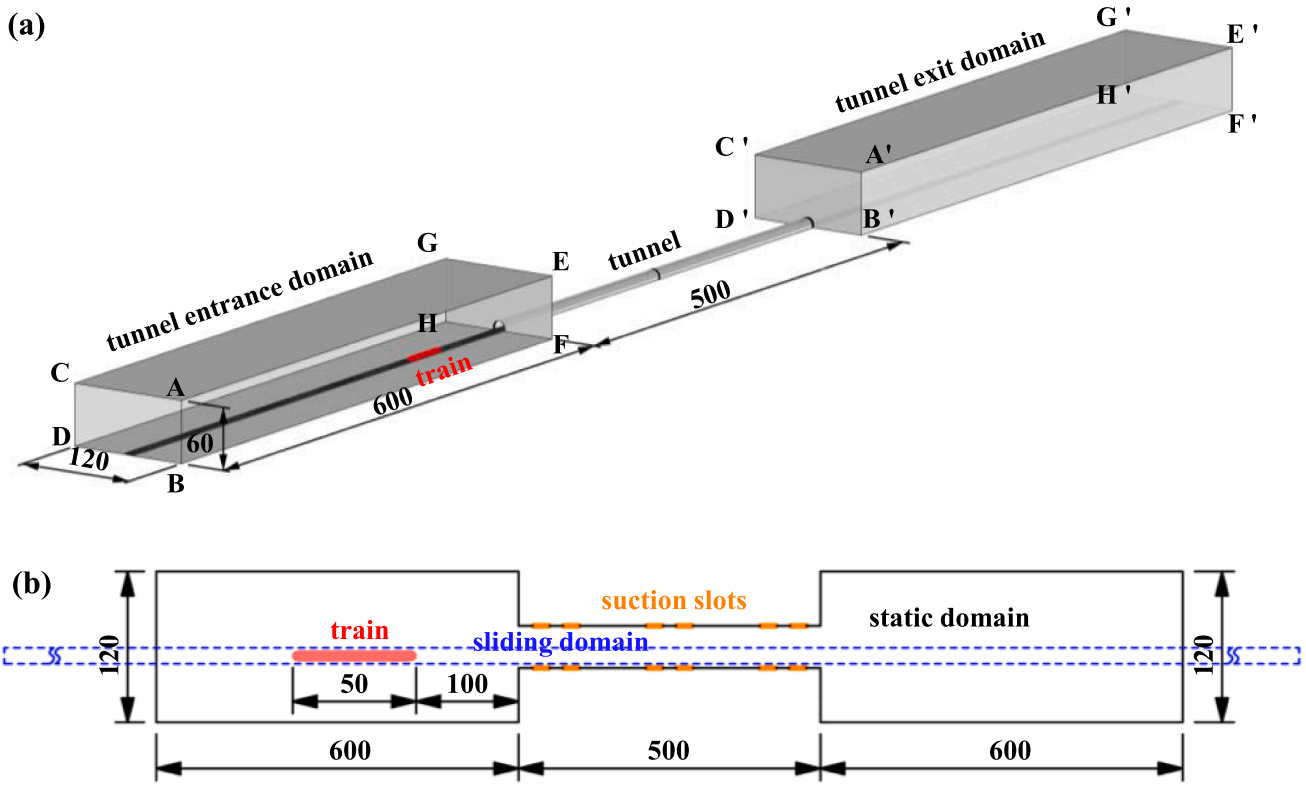

Fig. 3. (a) Computational domain and (b) sketch of different domain parts. (Unit: meter). (For interpretation of the references to color in this figure legend, the reader is referred to the web version of this article.)

119.44 m/s (i.e., the train's operating speed 430 km/h) to simulate the relative motion between the tunnel and maglev train. The interface boundary condition is used to exchange data between the sliding domain and the static domain.

3.2. Computational mesh and numerical scheme

A hybrid mesh is adopted in this study. A hexahedral mesh is constructed in all regions except the complex streamline region where a tetrahedral mesh is applied. Fig. 4 shows the surface mesh of the numerical model. Same as the meshing strategy used in earlier studies (Chen et al., 2017; Li et al., 2021a; Liu et al., 2019b; Yang et al., 2021), the size of the train surface cells ranges between 0.01 and 0.10 m. The cells around the actuation slots are refined (0.05 m) to preserve their geometric features and surrounding flow information. There are approximately 22 million computational cells in total.

ANSYS FLUENT 2020R2, a commercial computational fluid dynamics (CFD) software, is used to perform all the simulations in this study. The unsteady, compressible shear stress transport (SST) k-ω turbulence model is adopted, which was popular in previous studies on tunnel aerodynamic effects (Wang et al., 2021). The Semi-Implicit Method for Pressure-Linked Equations algorithm is employed for the pressure-velocity coupling, where the Least Squares Cell-based algorithm is chosen for computing the related gradient terms. The discretization schemes of all equations are second-order accuracy. The time advance process is implemented using the second-order implicit scheme. The physical advance time-step size from one iteration to the next is set as 0.005 s (Li et al., 2020; Liu et al., 2017; Niu et al., 2018), and the number of maximum iterations in each time-step is set as 30.

3.3. Validation of numerical scheme

The full-scale experimental data from Liu et al. (2019a) are used for the validation of the numerical scheme. The test adopted the China high-speed train CRH2, an eight-car train. In the test, the train passed through the 1921 m-long Pingtu tunnel (the efficient clearance area of the tunnel is 100 m^2) at 300 km/h. Using the same mesh-generating strategy and numerical settings described in Section 2.2, Fig. 5 compares the instantaneous pressure variations between the simulation and experimental results. The measuring point related to Fig. 5(a) is positioned at the middle of the fourth car of CRH2, and that related to Fig. 5 (b) is located in the tunnel and 415 m from the tunnel entrance portal. The results from the numerical simulation agree well with those from the full-scale experiment. The relative errors are all less than 10%, which are mainly because the simplification of the train model slightly alters the blocking ratio. Altogether, it is validated that the current mesh-generating scheme and numerical settings are feasible for this study.

4. Results and discussion

4.1. Flow structure analysis

To comprehend the impact of suction on the flow structures, Fig. 6 presents the flow structures in the tunnel under the unactuated and suction-actuated cases. Compared with those in the suction-actuated cases, the flow field of the unactuated case is relatively stable, and the pressure distribution is more uniform and closer to the atmospheric pressure. When the suction is actuated, the airflow near the suction slots is sucked away through the slots, thus forming a low-pressure region there. Fig. 7 further shows the evolution process of the flow structures during the passage of the train under the USV and SV50 cases. The high-pressure region generated by the entrance of the train is weakened under SV50, as shown in Fig. 7(a) and (b), since it is needed to overcome the flow field formed by the suction. In addition, at $t = 2.93$ s and $t = 5.00$ s, the high-pressure region in front of the train decreases significantly under SV50.

4.2. Transient pressure on the train surface

4.2.1. Pressure variation and distribution

Fig. 8 illustrates the process of pressure wave propagation at the measuring point H17 (at the middle of the middle car) under the USV and SV50 cases. In this figure, marks E and C denote the expansion and compression waves, respectively. Marks H and T represent the head and tail cars, respectively. Subscripts H and T refer to the pressure waves caused by the head and tail cars, while the number in subscripts signifies the number of reflections of pressure waves. The propagation of pressure waves in the tunnel under SV50 is consistent with that under USV, indicating that the suction does not affect the propagation of pressure waves. At $t = 0.84$ s, as the train nose enters the tunnel, C_{H1} is generated and propagates towards the exit at sonic speed. When C_{H1} reaches the tunnel exit portal at $t = 2.31$ s, one part of its energy is reflected to form E_{H2}, and the other part is emitted outside the tunnel as an MPW. Likewise, at $t = 1.26$ s, when the train tail enters the tunnel, E_{T1} is generated and propagates towards the entrance. At $t = 2.73$ s, C_{T2} is formed at the exit by the reflection of E_{T1}. For the instantaneous pressure at the measuring point H17, the pressure at H17 falls rapidly at $t = 1.37$ s when E_{T1} catches up to H17. Moreover, when the reflected pressure waves E_{H2} and C_{T2} meet H17 at $t = 3.07$ and 3.38 s, the pressure at H17 suffers a significant decrease and increase. The sudden pressure variations at H17 perfectly comply with the moment when the pressure waves act on the measuring point, indicating sufficient accuracy of the numerical simulation in the current study.

The instantaneous pressure variations at H1, H2 and H3 on the head car are shown in Fig. 9(a). H1 and H2 have a very high positive pressure value because they are close to the stagnation point of the head car, where the positive pressure is much stronger than the pressure variations induced by the pressure waves. However, for H3, the peak value of its first sudden pressure change (FSPC) is positive, but that of its second sudden pressure change (SSPC) is negative because there is a distance

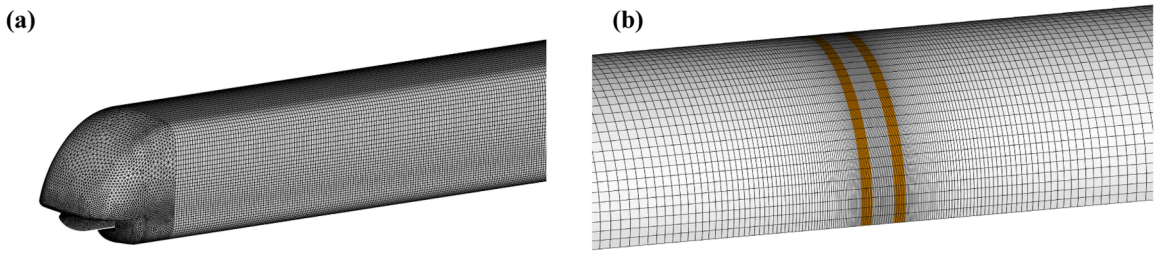

Fig. 4. (a) Train surface mesh and (b) tunnel and suction actuation slot surface mesh. (For interpretation of the references to color in this figure legend, the reader is referred to the web version of this article.)

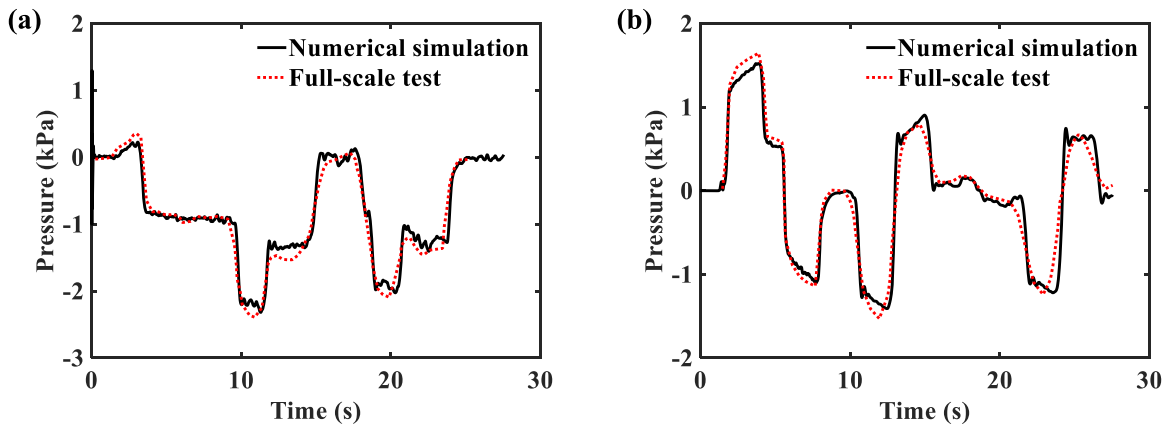

Fig. 5. Comparison of instantaneous pressure variations: (a) train surface and (b) tunnel surface. The full-scale test data are from Liu et al. (2019a). (For interpretation of the references to color in this figure legend, the reader is referred to the web version of this article.)

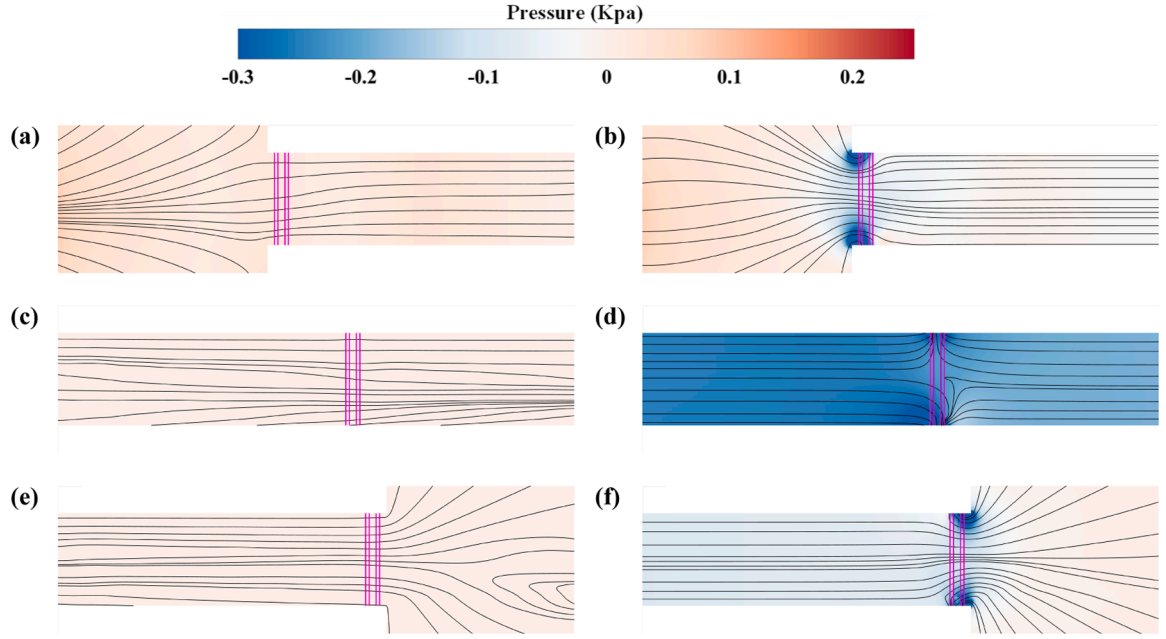

Fig. 6. Flow structures in the tunnel under the unactuated and suction-actuated cases: (a) the tunnel entrance portal under USV, (b) the tunnel entrance portal under SV50, (c) the middle of the tunnel under USV, (d) the middle of the tunnel under SV50, (e) the tunnel exit portal under USV, and (f) the tunnel exit portal under SV50. The section is at the train's half height, and the pink lines represent the locations of suction actuators. (For interpretation of the references to color in this figure legend, the reader is referred to the web version of this article.)

from the stagnation point. The pressures at H31, H32 and H33 on the tail car have similar trends. However, compared with those at H1, H2 and H3, the pressure amplitudes at H31, H32 and H33 are smaller, and even their FSPC disappears. In addition, Fig. 9(a) clearly shows the advantage of the suction flow control. On the one hand, the pressure amplitudes at H1, H2 and H3 experience a considerable reduction; on the other hand, the magnitudes of FSPC and SSPC at H1, H2 and H3 also have a significant reduction. As shown in Fig. 9(b), under SV50, there is a small drop in the magnitude of FSPC at H31, H32 and H33, and the pressure amplitudes at H31, H32 and H33 slightly decline after FSPC. Fig. 10 shows the instantaneous pressure variations near the streamline regions. The pressure near the streamline regions fluctuates in the negative pressure region because of the flow acceleration in these regions. After the suction is actuated, the pressure amplitudes near the streamline regions have an obvious increase, except for the region before FSPC.

Fig. 11 shows the instantaneous pressure variations at the measuring points H13, H14, H20 and H21, all of which are distributed at the train's half height. Because the pressure waves act on the measuring points in turn, there is a shift between the pressure variations at these measuring points. Furthermore, the pressure amplitudes at H15, H16, H17 and H18 progressively decrease from the head to the tail. Under SV50, there is a drop in the magnitudes of FSPC and SSPC at H13, H14, H20 and H21. Along the height direction, the pressure variations at H15, H16, H17 and H18 are shown in Fig. 12. Although the pressure variations at H15 (on the roof) are slightly different, the pressure variations at H16, H17 and H18 (on the side) nearly overlap. Similarly, the magnitudes of FSPC and SSPC at H15, H16, H17 and H18 decrease under SV50. In addition, Fig. 12 shows that the pressure amplitudes between FSPC and SSPC increase and the pressures after SSPC decrease, which can further reduce the pressure gradient near FSPC and SSPC.

4.2.2. *Effect of different suction velocities*

To further identify the influence of suction velocity, the instantaneous pressure variations at H1 (at the train nose and near the highest-pressure region) and H17 (at the middle of the train, which is less affected by the flow structures of the head and tail cars) under different

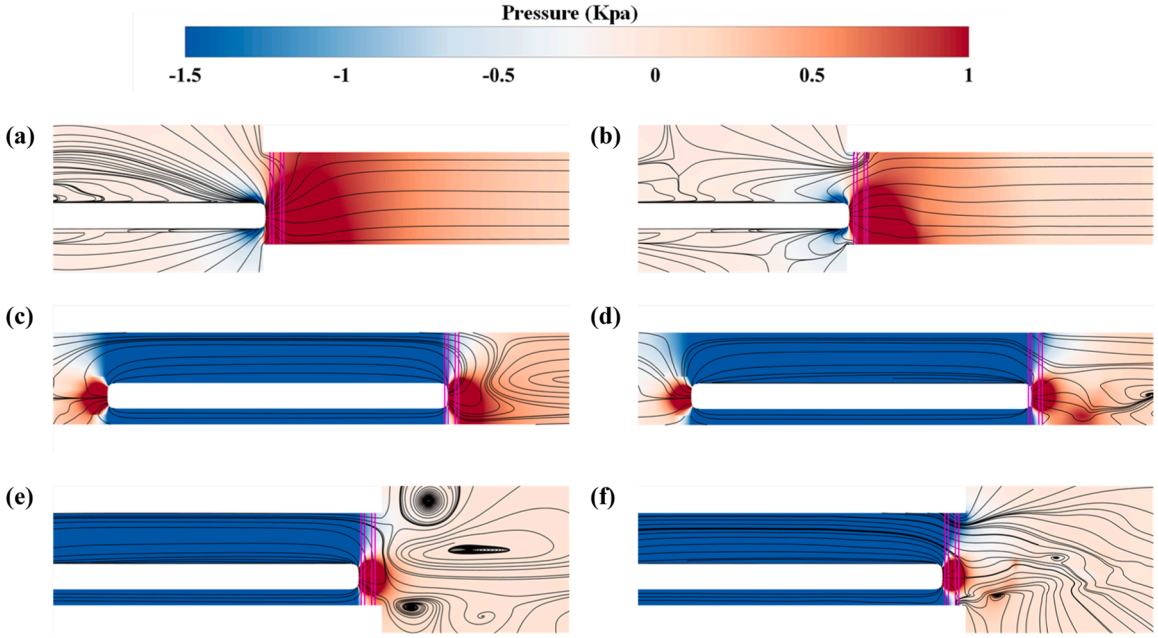

Fig. 7. Evolution process of the flow field during the passage of the train: (a) $t = 0.84$ s under USV, (b) $t = 0.84$ s under SV50, (c) $t = 2.93$ s under USV, (d) $t = 2.93$ s under SV50, (e) $t = 5.00$ s under USV, and (f) $t = 5.00$ s under SV50. The section is at the train's half-height, and the pink lines represent the locations of suction actuators. (For interpretation of the references to color in this figure legend, the reader is referred to the web version of this article.)

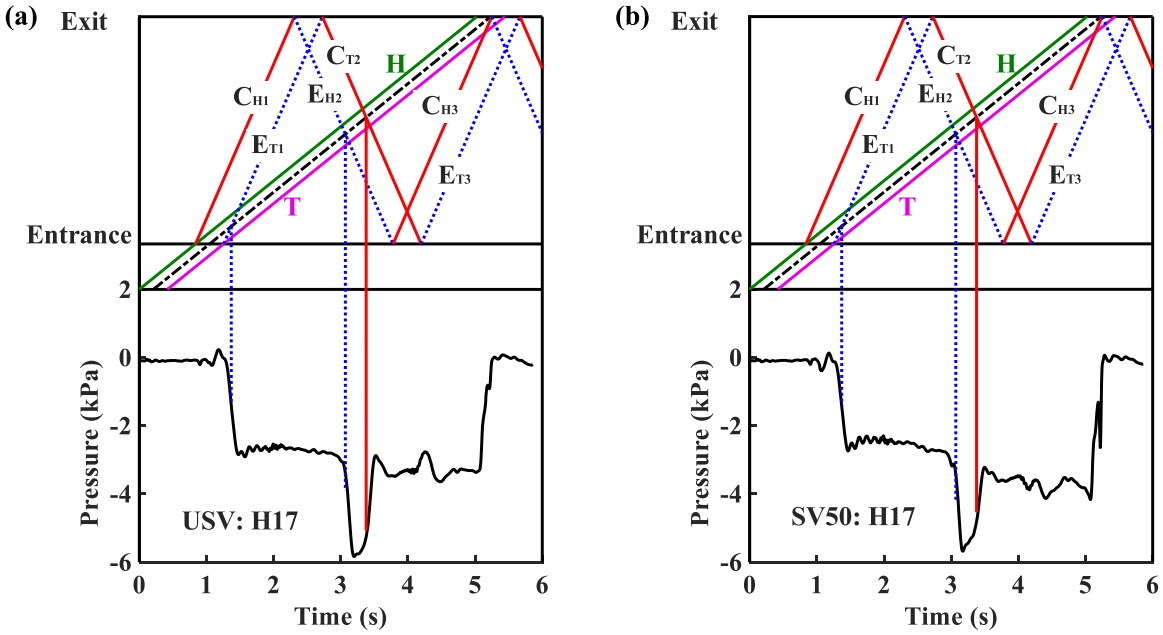

Fig. 8. Propagation of pressure waves at H17: (a) USV and (b) SV50. The upper part of the figures shows the pressure wave propagation, and the lower part of the figures shows the pressure variations at H17. (For interpretation of the references to color in this figure legend, the reader is referred to the web version of this article.)

suction velocities are presented in Fig. 13. For H1, the magnitude of FSPC and the pressure amplitudes in the region between FSPC and SSPC considerably decrease with increasing suction velocity. At the same time, the magnitude of SSPC and the pressure amplitudes in the region behind SSPC increase steadily, but the magnitude of SSPC changes little when the suction velocity increases from 30 m/s to 50 m/s. Compared with H1, the magnitude of FSPC at H17 experiences a smaller fall as the suction velocity increases. Moreover, the reduction in the magnitude of FSPC becomes smaller with increasing suction velocity. Similarly, the magnitude of SSPC at H17 increases slightly as the suction velocity increases, but the increase is small after the suction velocity reaches 30 m/s.

To gain a quantitative insight into the influence of suction velocity on the magnitudes of FSPC and SSPC, Fig. 14 shows the peak, valley, and peak-valley values of FSPC at H1 and H17 under different suction velocities. As depicted in Fig. 14(a) and (b), the peak and valley values of the FSPC have almost the same trend as the suction velocity, which means that the FSPC shifts up and down with the suction velocity, and the magnitude of the FSPC does not change considerably (see Fig. 14(e) and (f)). However, in Fig. 14(c) and (d), the peak values of SSPC at H1

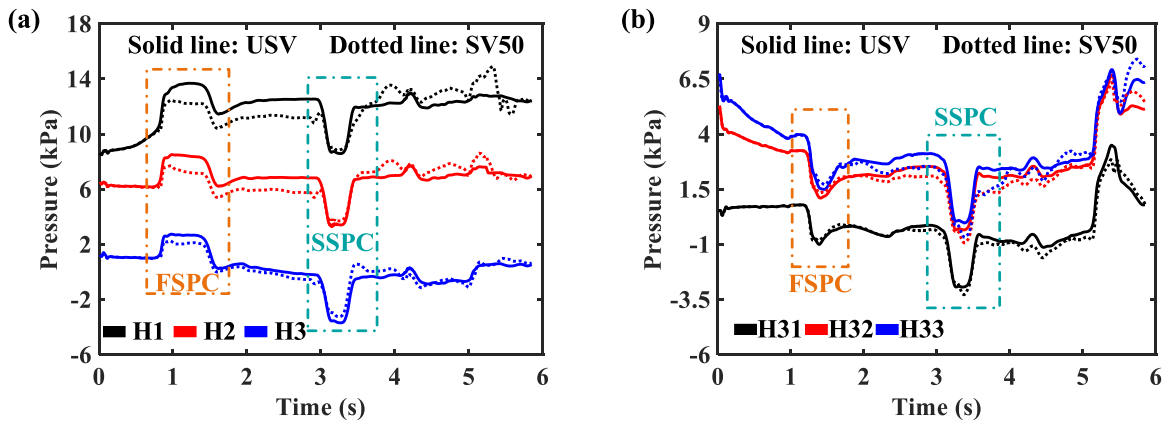

Fig. 9. Instantaneous pressure variations at measuring points near the stagnation points for (a) the head car and (b) the tail car. (For interpretation of the references to color in this figure legend, the reader is referred to the web version of this article.)

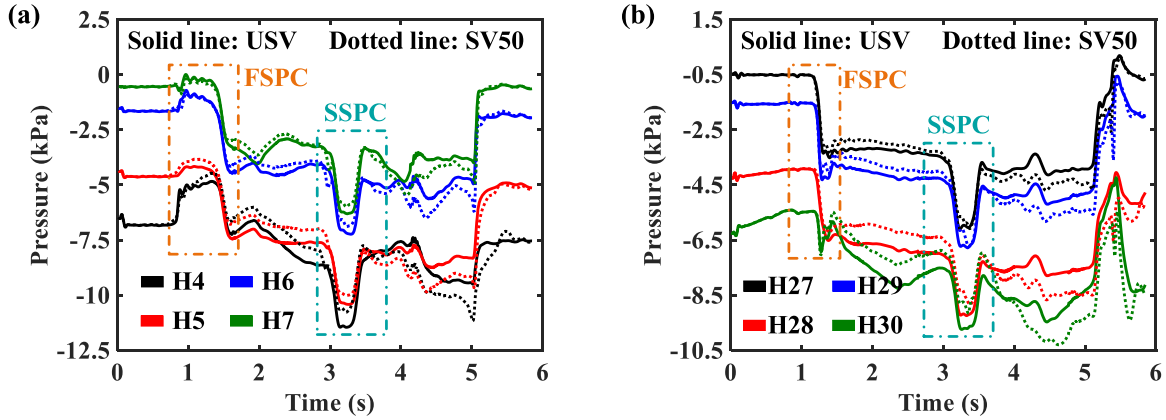

Fig. 10. Instantaneous pressure variations at measuring points near the streamlined regions for (a) the head car and (b) the tail car. (For interpretation of the references to color in this figure legend, the reader is referred to the web version of this article.)

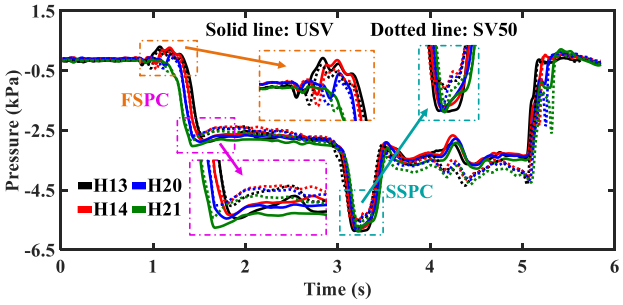

Fig. 11. Instantaneous pressure distributions along the longitudinal direction. (For interpretation of the references to color in this figure legend, the reader is referred to the web version of this article.)

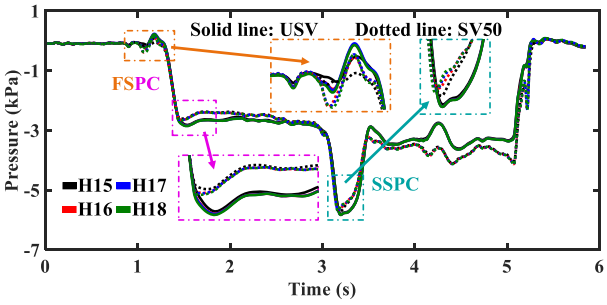

Fig. 12. Instantaneous pressure distributions along the vertical direction. (For interpretation of the references to color in this figure legend, the reader is referred to the web version of this article.)

and H17 decrease with increasing suction velocity, while the valley value of SSPC increases. Thus, the reduction of SSPC is relatively significant in Fig. 14(e) and (f), especially at H1.

To further quantify the alleviation effect of suction velocity on the sudden pressure changes, Table 1 compares the peak-valley values of FSPC and SSPC under different suction velocities, where the peak-valley values of FSPC and SSPC under USV are taken as a reference. As the suction velocity increases, a significant downward trend is observed in the magnitudes of SSPC at H1 and H17. For instance, under SV50, the magnitudes of SSPC at H1 and H17 decrease by 30.61% and 16.94%, respectively. However, the reduction of FSPC is quite limited. Although there are 10.44% and 6.82% drops in the magnitudes of FSPC at H1 and H17, respectively, the variations in FSPC between SV40 and SV50 do not exceed 1%, and even the magnitude of FSPC at H1 shows a small increase from SV40 to SV50.

4.3. *Transient pressure on the tunnel surface*

4.3.1. *Pressure variation and distribution*

Fig. 15 illustrates the process of pressure wave propagation at the tunnel surface measuring point T17 (the middle of the tunnel) under the USV and SV50 cases. The whole propagation process of the pressure

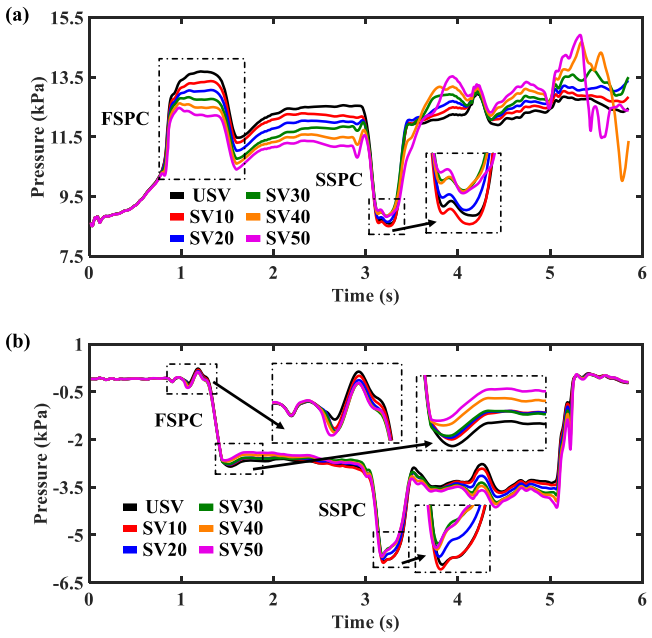

Fig. 13. Instantaneous pressure variations under different suction velocities: (a) H1 and (b) H17. (For interpretation of the references to color in this figure legend, the reader is referred to the web version of this article.)

waves is highly identical to that in Fig. 8, but the instantaneous pressure variations at the tunnel surface measuring points are different from those at the train surface measuring points. As illustrated in Fig. 15, there are three sudden pressure changes at T17, while H17 has only two (see Fig. 8). The first sudden pressure change (FSPC) occurs when the initial compression (C_{H1}) and expansion (E_{T1}) waves propagate successively to T17. Then, the second sudden pressure change (SSPC) is the cooperative effect of the train nose, the expansion wave (E_{H2}), the train tail, and the compression wave (C_{T2}) passing through T17 in succession. As the train nose passes by, there is a sharp drop in the pressure at T17, and this pressure will fall further when E_{H2} passes by. Thus, the magnitude of SSPC is much larger than that of FSPC. The third sudden pressure change (TSPC) is the result of successive passage of the compression (C_{H3}) and expansion (E_{T3}) waves.

Fig. 16 shows the instantaneous pressure variations of the measuring points T3, T9, T17, T23 and T31. These measuring points are at half the train height, where T3, T17 and T31 are distributed between each pair of actuation slots, while T9 and T23 are in the middle of two pairs of actuation slots. As shown in Fig. 16, the instantaneous pressure variations of these measuring points are distinct because of different locations of the measuring points. For example, SSPC at T17 in Fig. 15 is the superposition effect caused by the passage of the train and pressure waves; but in other measuring points, SSPC is split into two negative sudden pressure changes, and the distance between them changes as the measuring point approaches the tunnel exit. On the magnitude of FSPC, T31 is the smallest (near the tunnel exit portal), followed by T3 (near the tunnel entrance portal), and finally by T9, T17 and T23 (closer to the middle of the tunnel). In addition, suction can significantly reduce the magnitude of FSPC, which is one of the main indices for evaluating the magnitude of the pressure waves (Han et al., 2022; Li et al., 2022a; Xiong et al., 2020). Nevertheless, a comparison of the instantaneous pressure variations at T9, T17 and T23 (points in the front, middle and rear of middle suction actuators) tells that the reductions of FSPC at these measuring points are almost the same, which means that the alleviation effect of suction on the tunnel wall cannot be accumulated.

To further reveal the tunnel surface pressure variations before and after actuating the suction, Fig. 17(a) shows the instantaneous pressure variations at T13, T16 and T19, which are located at both the sides and middle of the middle suction actuators. As shown in Fig. 17(a), under SV50, the magnitudes of FSPC, SSPC and TSPC at these measuring points suffer a dramatic decrease, except that the magnitude of SSPC at T19 increases slightly, which is caused by the superposition effect shown in Fig. 16. In addition, the magnitudes of FSPC at the measuring points are almost the same before the suction is actuated, but the reductions of FSPC at these points are slightly different after the suction is actuated. The reduction of FSPC in the middle of the suction actuators (T16) is the largest, while the reduction in the front of suction actuators (T13) is greater than that in the rear of the suction actuators (T19). Fig. 17(b) shows the instantaneous pressure variations at T15, T16 and T17. Under SV50, the pressure variations at the measuring points basically overlap like those under USV, indicating that the pressure waves still propagate in one dimension after the suction is actuated.

4.3.2. *Effect of different suction velocities*

Fig. 18 shows the instantaneous pressure variation at T17 under different suction velocities. The absolute pressure at T17 decreases when the suction is actuated, especially the magnitudes of FSPC, SSPC and TSPC. However, the absolute pressure at T17 does not decrease significantly. There is a tiny difference between the pressure curves under USV and SV10. When the suction velocity increases from 10 m/s to 30 m/s, the absolute pressure at T17 decreases obviously. After the suction velocity increases to 40 m/s or 50 m/s, the decreasing rate of the absolute pressure at T17 becomes slower, which is similar to the train surface pressure variations shown in Fig. 13(b).

As shown in Fig. 19, although FSPC and TSPC have similar magnitudes, the alleviation effect of suction on them is slightly different. When the suction velocity increases, the peak value of TSPC decreases faster than that of FSPC, so the downtrend of the magnitude of TSPC is more obvious than that of FSPC (see Fig. 19(a) and (c)). Furthermore, as the suction velocity increases, the downtrend of the magnitude of SSPC is the steepest (see Fig. 19(d)) because the trends of its peak and valley values are opposite (see Fig. 19(b)), which greatly decreases the peak-valley value of SSPC. Table 2 lists the reduction percentage of sudden pressure change at T17 under different suction velocities, with the value from USV as a reference. When the suction velocity increases to 50 m/s, the magnitude of TSPC decreases significantly by 32.02%, while those of FSPC and SSPC decrease by 14.95% and 15.96%, respectively. In addition, unlike the train surface sudden pressure changes, when the suction velocity increases from 40 m/s to 50 m/s, the variation of the tunnel surface sudden pressure changes is still larger than 1%, meaning that there is space to further increase suction velocity to alleviate the tunnel surface sudden pressure changes.

4.4. *MPW at the tunnel exit*

One part of the “head wave”, i.e., initial compression wave (ICW) C_{H1}, radiates as an MPW at the tunnel exit, causing noise pollution. Fig. 20 shows the MPW at the measuring points M1 to M7 under the USV and SV50 cases. The amplitude of the MPW decreases as the distance from the exit increases either under USV or SV50. However, under SV50, the amplitudes of the MPW at each measuring point obviously decrease. The effect of suction gradually weakens with increasing distance from the exit. For example, the reduction of amplitude of the MPW is obvious at M1, but it is difficult to observe at M9, as shown in Fig. 20(b).

According to previous studies (Fukuda et al., 2006; Standardization, 2018), the magnitude of the MPW is approximately proportional to the pressure gradient of the ICW. Fig. 21 shows both the wavefront of the ICW and its pressure gradient at T17. The wavefront of the ICW at T17 decreases as the suction velocity increases, and its pressure gradient decreases accordingly. Finally, as displayed in Fig. 22, the amplitude of the MPW is alleviated. Herein, the amplitudes of MPWs at M2 and M5 are selected for analysis since they are key indices used to measure the intensity of noise pollution (Han et al., 2022; Zhang et al., 2017). As shown in Fig. 22, the amplitudes of the MPW at M2 and M5 decrease as

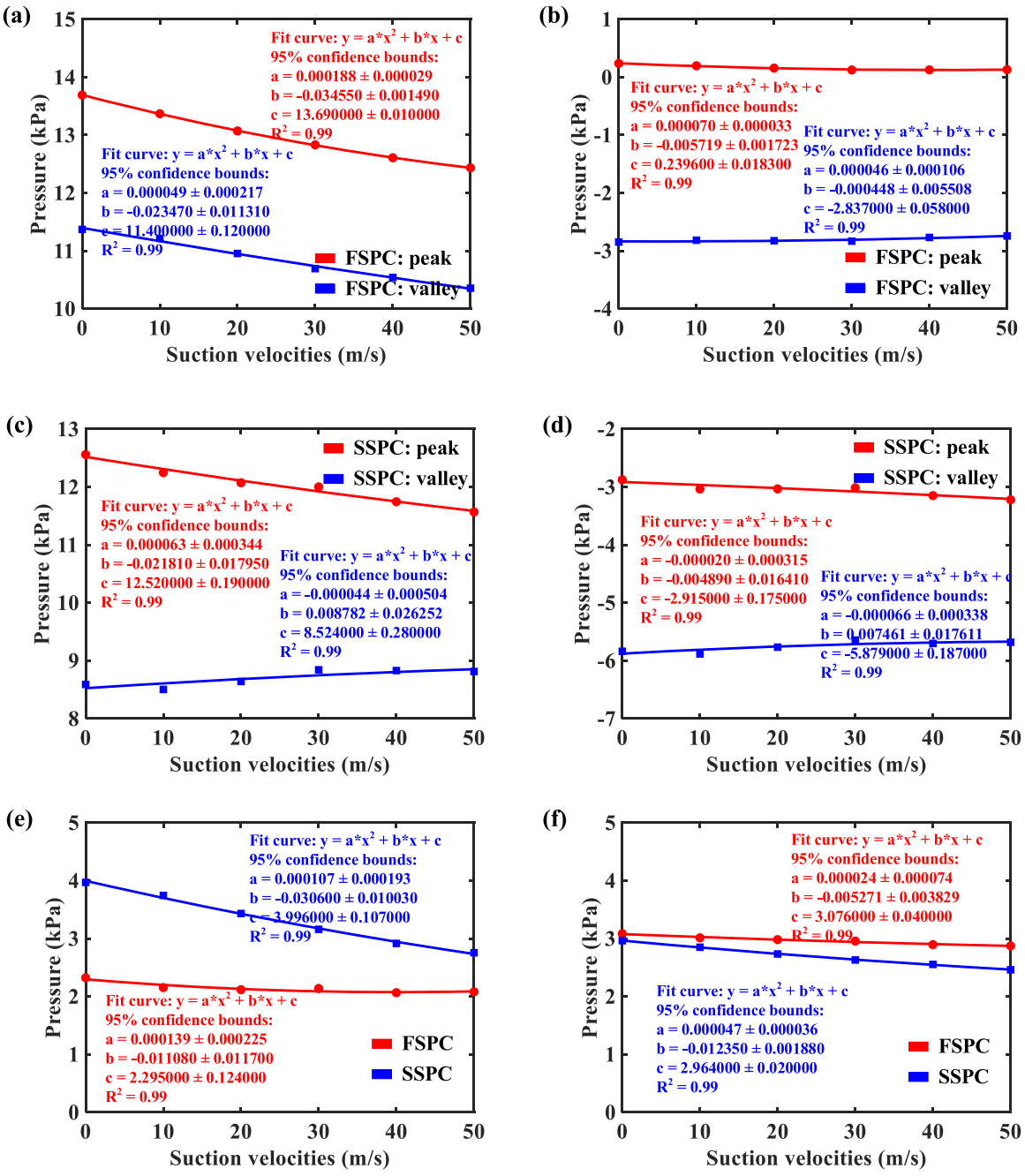

Fig. 14. The peak, valley and peak-valley values of FSPC and SSPC versus suction velocity: (a) the peak and valley values of FSPC at H1, (b) the peak and valley values of FSPC at H17, (c) the peak and valley values of SSPC at H1, (d) the peak and valley values of SSPC at H17, (e) the peak-valley values of FSPC and SSPC at H1, and (f) the peak-valley values of FSPC and SSPC at H17. (For interpretation of the references to color in this figure legend, the reader is referred to the web version of this article.)

Table 1
Comparison of the peak-valley values of FSPC and SSPC under different suction velocities.

Measuring points	Sudden pressure change	USV	SV10	SV20	SV30	SV40	SV50
H1	FSPC	\	−7.29%	−8.87%	−7.95%	−11.06%	−10.44%
	SSPC	\	−5.67%	−13.54%	−20.43%	−26.56%	−30.61%
H17	FSPC	\	−2.32%	−3.34%	−4.15%	−6.14%	−6.82%
	SSPC	\	−3.81%	−7.74%	−11.24%	−13.82%	−16.94%

the suction velocity increases, but the amplitude of the MPW at M2 decreases more than that at M5, as shown in Fig. 20. The relationship between the amplitude of the MPW and the suction velocity is shown in Fig. 23, and Table 3 lists in detail the reduction in the MPW. Compared to those under USV, the amplitudes of the MPW under SV50 at M2 and M5 decrease by 12.44% and 11.91%, respectively.

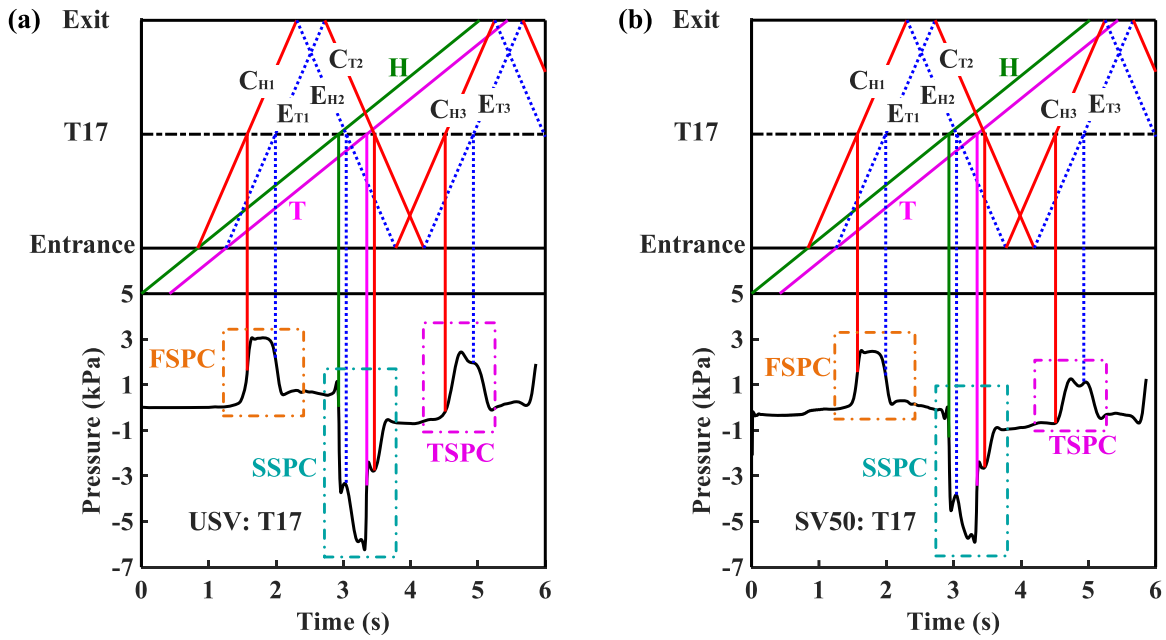

Fig. 15. Propagation of pressure waves at T17: (a) USV and (b) SV50. The upper part of the figures shows the pressure wave propagation, and the lower part of the figures shows the pressure variations at T17. (For interpretation of the references to color in this figure legend, the reader is referred to the web version of this article.)

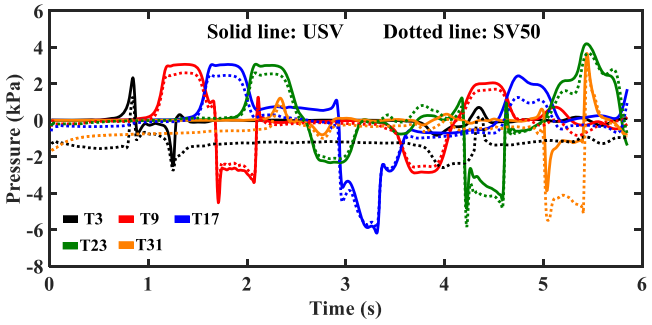

Fig. 16. Instantaneous pressure variations at the measuring points along the tunnel. (For interpretation of the references to color in this figure legend, the reader is referred to the web version of this article.)

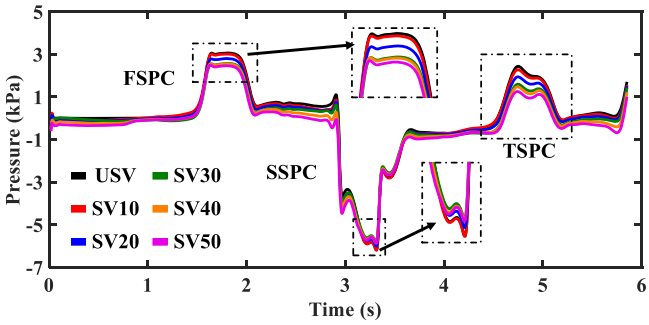

Fig. 18. Instantaneous pressure variations at T17 under different suction velocities. (For interpretation of the references to color in this figure legend, the reader is referred to the web version of this article.)

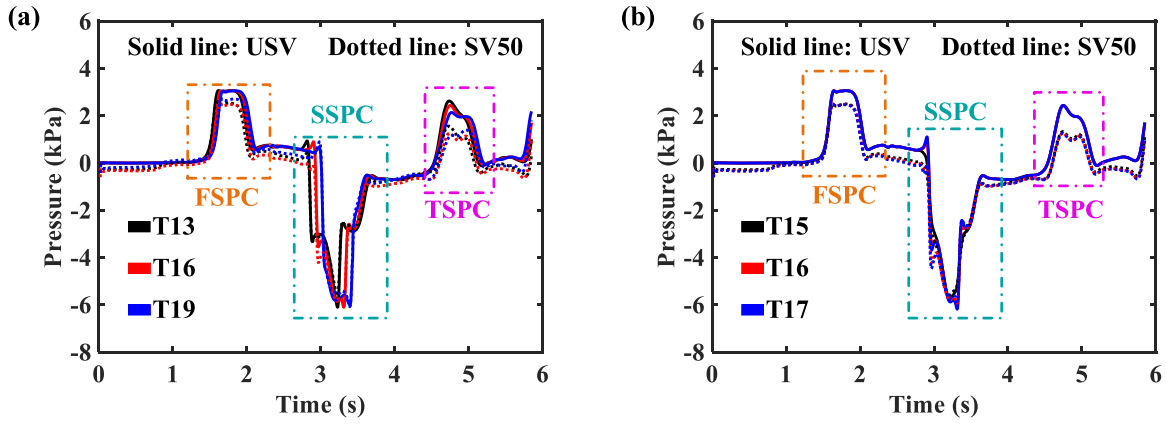

Fig. 17. Instantaneous pressure variations at the measuring points: (a) around the suction actuators, and (b) in the middle section of the tunnel. (For interpretation of the references to color in this figure legend, the reader is referred to the web version of this article.)

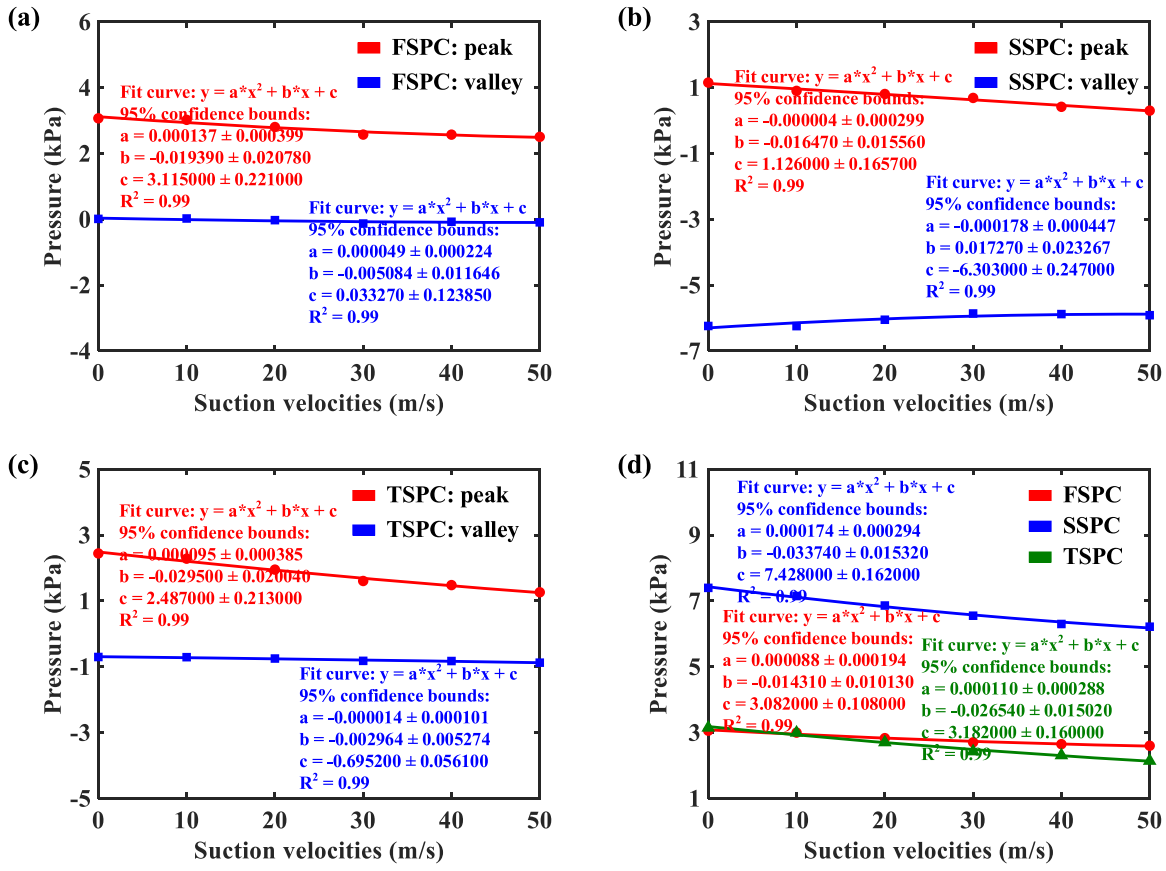

Fig. 19. The peak, valley and peak-valley values of FSPC, SSPC and TSPC at measuring point T17 versus suction velocity: (a) the peak and valley values of FSPC, (b) the peak and valley values of SSPC, (c) the peak and valley values of TSPC, and (d) the peak-valley values of FSPC, SSPC and TSPC. (For interpretation of the references to color in this figure legend, the reader is referred to the web version of this article.)

Table 2
Comparison of the peak-valley values of FSPC, SSPC and TSPC at T17 under different suction velocities.

Measuring points	Pressure sudden change	USV	SV10	SV20	SV30	SV40	SV50
T17	FSPC	\	−1.90%	−7.39%	−11.54%	−13.37%	−14.95%
	SSPC	\	−3.34%	−7.25%	−11.44%	−14.84%	−15.96%
	TSPC	\	−4.87%	−14.13%	−22.88%	−26.67%	−32.02%

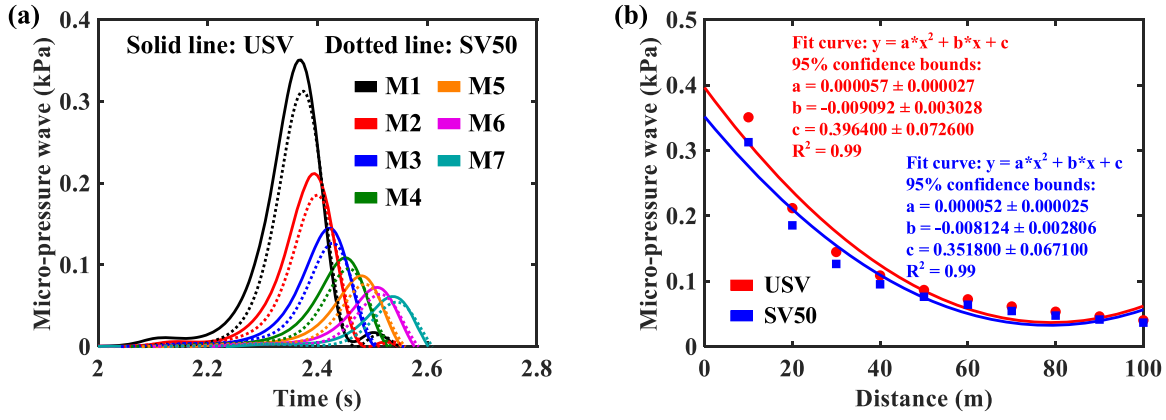

Fig. 20. (a) Distributions of the MPW at the tunnel exit and (b) variations of the MPW with distance. (For interpretation of the references to color in this figure legend, the reader is referred to the web version of this article.)

5. Conclusions

In this study, the application of the suction flow method on a tunnel wall under different suction velocities has been investigated using a compressible, unsteady, SST $k-\omega$ turbulence model. The suction actuators are positioned near the entrance, middle and exit of the tunnel

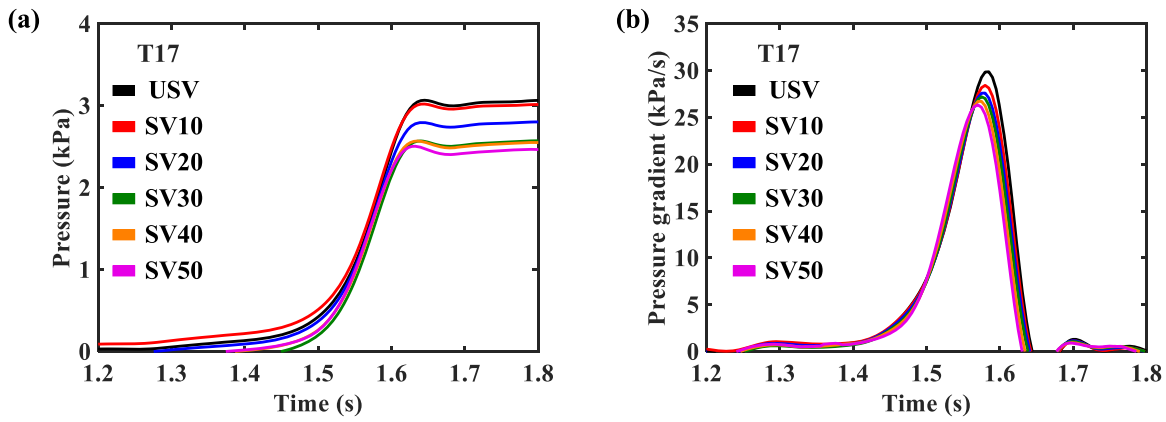

Fig. 21. (a) Wavefront of the ICW and (b) pressure gradient of the ICW at T17 under different suction velocities. (For interpretation of the references to color in this figure legend, the reader is referred to the web version of this article.)

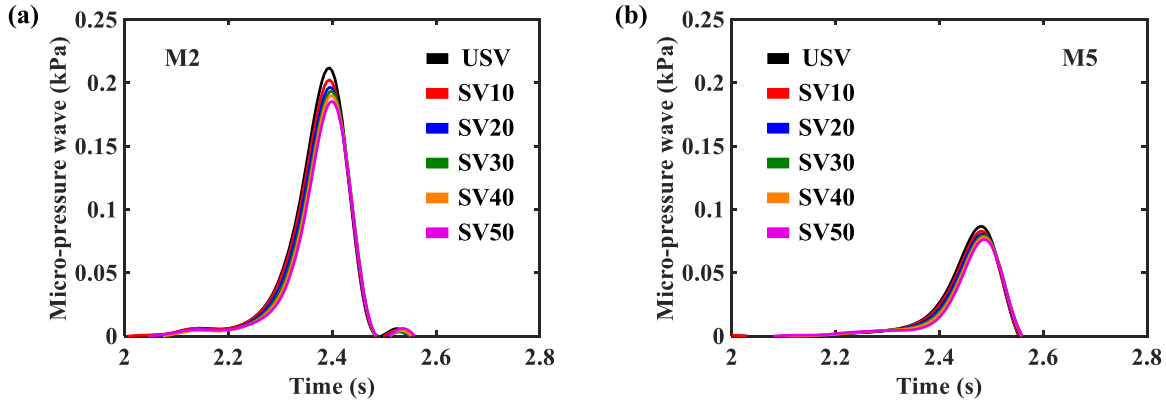

Fig. 22. MPW under different suction velocities at (a) M2 and (b) M5. (For interpretation of the references to color in this figure legend, the reader is referred to the web version of this article.)

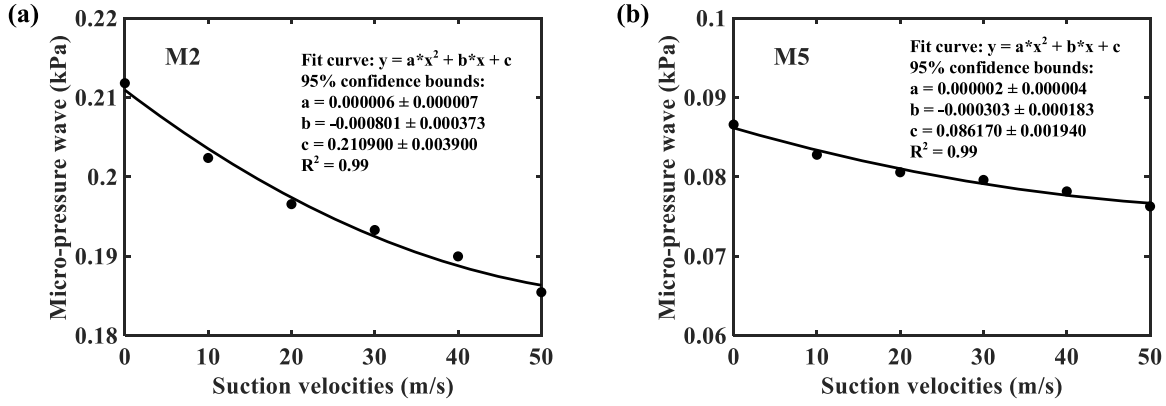

Fig. 23. Variations of the MPW versus suction velocity.

Table 3
Comparison of the amplitudes of MPW under different suction velocities.

Measuring points	USV	SV10	SV20	SV30	SV40	SV50
M2	\	−4.45%	−7.20%	−8.74%	−10.31%	−12.44%
M5	\	−4.40%	−6.95%	−8.06%	−9.73%	−11.91%

with intent to reduce the tunnel aerodynamic effects through altering the generation, propagation, and emission of pressure waves. The main conclusions obtained from this study are as follows:

(1) The suction has an obvious influence on the pressure distribution. A low-pressure region is formed near the suction slots after the suction is actuated. As the train and pressure waves pass through the low-pressure region, a part of the positive pressure can be canceled out; thus, the high-pressure region in front of the train and the ICW are obviously diminished;

(2) Compared with the unactuated case, the suction-actuated cases are proven helpful in improving the train surface pressure, tunnel surface pressure, and MPW. Upon reaching a suction velocity of 50 m/s, the FSPC and SSPC of the train surface pressure at H1 suffer significant reductions by 10.44% and 30.61%, respectively; the FSPC, SSPC and TSPC of the tunnel surface pressure at T17 decrease by 14.95%, 15.96% and 32.02%, respectively; the MPW at M2 and M5 decrease by 12.44% and 11.91%, respectively.
(3) The effectiveness of the suction method in alleviating the interactive aerodynamics between the train and tunnel gradually increases with an increase in suction velocity. It is worth noting that the suction method has a greater impact on mitigating the tunnel surface sudden pressure and MPW than mitigating train surface sudden pressure. Moreover, while the variation in train surface sudden pressure is negligible as the suction velocity increases from 40 m/s to 50 m/s, there is still room for further mitigation of tunnel surface sudden pressure and MPW through further increases in the suction velocity.

The current work reveals the capability of the suction technique in alleviating the tunnel aerodynamic effect. However, as observed in the evaluation of the tunnel surface pressure, the alleviation effect of multiple suction slots cannot be accumulated. Therefore, there is a need for further studies on the distribution and dimension of suction slots in future.

Declaration of Competing Interest

The authors declare that they have no known competing financial interests or personal relationships that could have appeared to influence the work reported in this paper.

Data availability

Data will be made available on request.

Acknowledgements

This work was supported by the National Natural Science Foundation of China (Grant No. 52202426, 52105523), the Open Project of Key Laboratory of Traffic Safety on Track of Ministry of Education, Central South University (Grant No. 502401002), Start-up Fund for RAPs under the Strategic Hiring Scheme of The Hong Kong Polytechnic University (Grant No. 1-BD23), the Natural Science Foundation of Hunan Province, China (Grant No. 2020JJ4737), the Natural Science Foundation of Shandong (Grant No. ZR2021QE249). The work described in this paper was also supported by a grant (RIF) from the Research Grants Council of the Hong Kong Special Administrative Region (SAR), China (Grant No. R-5020-18) and a grant from the National Natural Science Foundation of China (Grant No. U1934209). The authors would also like to appreciate the funding support by the Innovation and Technology Commission of the Hong Kong SAR Government (Grant No. K-BBY1), and the Hong Kong and Macau Joint Research and Development Fund of Wuyi University (Grants No. 2019WGALH15, 2019WGALH17, 2021WGALH15), and Guangdong Basic and Applied Basic Research Fund for Guangdong-Hong Kong-Macao Research Team Project (Grant No. 2021B1515130006).

References

Chehri, A., & Mouftah, H. T. (2019). Autonomous vehicles in the sustainable cities, the beginning of a green adventure. *Sustainable Cities and Society, 51*, Article 101751. https://doi.org/10.1016/j.scs.2019.101751

Chen, Z., Liu, T., Zhou, X., & Niu, J. (2017). Impact of ambient wind on aerodynamic performance when two trains intersect inside a tunnel. *Journal of Wind Engineering and Industrial Aerodynamics, 169*, 139–155. https://doi.org/10.1016/j.jweia.2017.07.018

Chen, Z., Ni, Y., Wang, Y., Wang, S., & Liu, T. (2022). Mitigating crosswind effect on high-speed trains by active blowing method: A comparative study. *Engineering Applications of Computational Fluid Mechanics, 16*(1), 1064–1081. https://doi.org/10.1080/19942060.2022.2064921

Dogaroglu, B., Caliskanelli, S. P., & Tanyel, S. (2021). Comparison of intelligent parking guidance system and conventional system with regard to capacity utilisation. *Sustainable Cities and Society, 74*, Article 103152. https://doi.org/10.1016/j.scs.2020.102594

Dong, F., Huang, Z., Hao, L., Xu, X., Jin, Z., & Shao, N. (2019). An on-board 2 G HTS magnets system with cooling-power-free and persistent-current operation for ultrahigh speed superconducting maglevs. *Scientific Reports, 9*(1), 11844. https://doi.org/10.1038/s41598-019-48136-x

Fang, X., Lin, S., Yang, Z., Lin, F., Sun, H., & Hu, L. (2018). Adhesion control strategy based on the wheel-rail adhesion state observation for high-speed trains. *Electronics, 7*(5), 70. https://doi.org/10.3390/electronics7050070

Fukuda, T., Ozawa, S., Iida, M., Takasaki, T., & Wakabayashi, Y. (2006). Distortion of compression wave propagating through very long tunnel with slab tracks. *JSME International Journal Series B Fluids and Thermal Engineering, 49*(4), 1156–1164. https://doi.org/10.1299/jsmeb.49.1156

Gillani, S. A., Panikulam, V. P., Sadasivan, S., & Yaoping, Z. (2019). CFD Analysis of aerodynamic drag effects on vacuum tube trains. *Journal of Applied Fluid Mechanics, 12*(1), 303–309. https://doi.org/10.29252/jafm.75.253.29091

Guo, Y., Yang, L., Lu, Y., & Zhao, R. (2021). Dockless bike-sharing as a feeder mode of metro commute? The role of the feeder-related built environment: Analytical framework and empirical evidence. *Sustainable Cities and Society, 65*, Article 102594. https://doi.org/10.1016/j.scs.2020.102594

Han, H. S., & Kim, D. S. (2016). *Magnetic levitation : Maglev technology and applications, 13*. Springer.

Han, J. B., & Kim, K. J. (2018). Characteristics of vibration in magnetically levitated trains subjected to crosswind. *Proceedings of the Institution of Mechanical Engineers, Part F: Journal of Rail and Rapid Transit, 232*(5), 1347–1359. https://doi.org/10.1177/0954409717721378

Han, S., Zhang, J., Xiong, X., Ji, P., Zhang, L., Sheridan, J., & Gao, G. (2022). Influence of high-speed maglev train speed on tunnel aerodynamic effects. *Building and Environment, 223*, Article 109460. https://doi.org/10.1016/j.buildenv.2022.109460

Kellermann, R., Biehle, T., & Fischer, L. (2020). Drones for parcel and passenger transportation: A literature review. *Transportation Research Interdisciplinary Perspectives, 4*, Article 100088. https://doi.org/10.1016/j.trip.2019.100088

Kim, D. H., Cheol, S. Y., Iyer, R. S., & Kim, H. D. (2021a). A newly designed entrance hood to reduce the micro pressure wave emitted from the exit of high-speed railway tunnel. *Tunnelling and Underground Space Technology, 108*, Article 103728. https://doi.org/10.1016/j.tust.2020.103728

Kim, D. H., Seo, Y. C., Kim, T. H., & Kim, H. D. (2021b). Effects of detailed shape of air-shaft entrance hood on tunnel pressure waves. *Journal of Mechanical Science and Technology, 35*(2), 615–624. https://doi.org/10.1007/s12206-021-0121-3

Li, C., Liu, M., Chang, R., Wang, X., Liu, W., & Zhang, H. (2022a). Air pressure and comfort study of the high-speed train passing through the subway station. *Sustainable Cities and Society, 81*, Article 103881. https://doi.org/10.1016/j.scs.2022.103881

Li, Q., & Chen, C. (2019). Survey and measurement of the vehicle pollutant emission in urban underground bifurcate tunnel, China. *Sustainable Cities and Society, 48*, Article 101519. https://doi.org/10.1016/j.scs.2019.101519

Li, W., Liu, T., Chen, Z., Guo, Z., & Huo, X. (2020). Comparative study on the unsteady slipstream induced by a single train and two trains passing each other in a tunnel. *Journal of Wind Engineering and Industrial Aerodynamics, 198*, Article 104095. https://doi.org/10.1016/j.jweia.2020.104095

Li, W., Liu, T., Huo, X., Chen, Z., Guo, Z., & Li, L. (2019). Influence of the enlarged portal length on pressure waves in railway tunnels with cross-section expansion. *Journal of Wind Engineering and Industrial Aerodynamics, 190*, 10–22. https://doi.org/10.1016/j.jweia.2019.03.031

Li, W., Liu, T., Martinez-Vazquez, P., Chen, Z., Guo, Z., Li, M., Xia, Y., & Liu, H. (2021a). Aerodynamic effects of a high-speed train travelling through adjoining & separated tunnels. *Tunnelling and Underground Space Technology, 113*, Article 103973. https://doi.org/10.1016/j.tust.2021.103973

Li, W., Liu, T., Martinez-Vazquez, P., Chen, Z., Huo, X., & Guo, Z. (2021b). Influence of blockage ratio on slipstreams in a high-speed railway tunnel. *Tunnelling and Underground Space Technology, 115*, Article 104055. https://doi.org/10.1016/j.tust.2021.104055

Li, W., Liu, T., Martinez-Vazquez, P., Xia, Y., Chen, Z., & Guo, Z. (2022b). Aerodynamic effects on a railway tunnel with partially changed cross-sectional area. *Journal of Central South University, 29*(8), 2589–2604. https://doi.org/10.1007/s11771-022-5113-7

Lin, G., & Sheng, X. (2018). Application and further development of Maglev transportation in China. *Transportation Systems and Technology, 4*(3), 36–43.

Lin, Y., Qin, Y., Wu, J., & Xu, M. (2021). Impact of high-speed rail on road traffic and greenhouse gas emissions. *Nature Climate Change, 11*(11), 952–957. https://doi.org/10.1038/s41558-021-01190-8

Liu, F., Zhou, W., Niu, J., & Zhang, J. (2019a). Impact of increased linings on pressure transients induced by a train passing through a tunnel. *Sustainable Cities and Society, 45*, 314–323. https://doi.org/10.1016/j.scs.2018.10.030

Liu, T., Chen, Z., Chen, X., Xie, T., & Zhang, J. (2017). Transient loads and their influence on the dynamic responses of trains in a tunnel. *Tunnelling and Underground Space Technology, 66*, 121–133. https://doi.org/10.1016/j.tust.2017.04.009

Liu, T., Jiang, Z., Li, W., Guo, Z., Chen, X., Chen, Z., & Krajnovic, S. (2019b). Differences in aerodynamic effects when trains with different marshalling forms and lengths

enter a tunnel. *Tunnelling and Underground Space Technology, 84*, 70–81. https://doi.org/10.1016/j.tust.2018.10.016

Luo, J., Li, Z., Wang, L., Zhang, D., & Wu, Y. (2020). Aerodynamic effect of cross passages at the entrance section of a high-speed railway tunnel in a region with mountains and canyons. *Journal of Wind Engineering and Industrial Aerodynamics, 204*, Article 104268. https://doi.org/10.1016/j.jweia.2020.104268

Meng, S., Li, X., Chen, G., Zhou, D., Chen, Z., & Krajnovic, S. (2021). Numerical simulation of slipstreams and wake flows of trains with different nose lengths passing through a tunnel. *Tunnelling and Underground Space Technology, 108*, Article 103701. https://doi.org/10.1016/j.tust.2020.103701

Minelli, G., Yao, H. D., Andersson, N., Lindblad, D., Forssén, J., Höstmad, P., & Krajnović, S. (2021). Using horizontal sonic crystals to reduce the aeroacosutic signature of a simplified ICE3 train model. *Applied Acoustics, 172*, Article 107597. https://doi.org/10.1016/j.apacoust.2020.107597

Miyachi, T., & Fukuda, T. (2021). Model experiments on area optimization of multiple openings of tunnel hoods to reduce micro-pressure waves. *Tunnelling and Underground Space Technology, 115*, Article 103996. https://doi.org/10.1016/j.tust.2021.103996

Niu, J., Zhou, D., Liang, X., Liu, S., & Liu, T. (2018). Numerical simulation of the Reynolds number effect on the aerodynamic pressure in tunnels. *Journal of Wind Engineering and Industrial Aerodynamics, 173*, 187–198. https://doi.org/10.1016/j.jweia.2017.12.013

Okubo, H., Miyachi, T., & Takashi, F. (2022). Field test for micro-pressure wave reduction measurement by area optimization of windows of tunnel hoods. *Proceedings of the Institution of Mechanical Engineers, Part F: Journal of Rail and Rapid Transit, 236*(10), 1262–1270. https://doi.org/10.1177/09544097221080368

Saito, S., Miyachi, T., & Iida, M. (2013). Countermeasure for reducing micro-pressure wave emitted from railway tunnel by installing hood at the exit of tunnel. *Quarterly Report of RTRI, 54*(4), 231–236. https://doi.org/10.2219/rtriqr.54.231

Schmid, P., Schneider, G., Dignath, F., Liang, X., & Eberhard, P. (2021). Static and dynamic modeling of the electromagnets of the maglev vehicle transrapid. *IEEE Transactions on Magnetics, 57*(2), 1–15. https://doi.org/10.1109/TMAG.2020.3039950

Schmutzler, A. (2021). The hidden benefits of high-speed rail. *Nature Climate Change, 11*(11), 902–903. https://doi.org/10.1038/s41558-021-01199-z

Shi, Y., Ma, W., Li, M., & Xu, Z. (2022). Research on dynamics of a new high-speed maglev vehicle. *Vehicle System Dynamics, 60*(3), 721–742. https://doi.org/10.1080/00423114.2020.1838568

Standardization, E.C.f. (2018). Railway applications - Aerodynamics - Part 5: Requirements and test procedures for aerodynamics in tunnels: EN 14067-6. https://doi.org/10.1299/jsmeb.49.1156.

Sun, Z. X., Wang, M. Y., Wei, L. Y., Kong, F. B., & Yang, G. W. (2021). Aerodynamic shape optimization of an urban maglev train. *Acta Mechanica Sinica, 37*(6), 954–969. https://doi.org/10.1007/s10409-021-01094-y

Vuchic, V. R., & Casello, J. M. (2002). An evaluation of maglev technology and its comparison with high speed rail. *Transportation Quarterly, 56*(2), 33–49.

Wang, L., Luo, J., Li, F., Guo, D., Gao, L., & Wang, D. (2021). Aerodynamic performance and flow evolution of a high-speed train exiting a tunnel with crosswinds. *Journal of Wind Engineering and Industrial Aerodynamics, 218*, Article 104786. https://doi.org/10.1016/j.jweia.2021.104786

Wang, T., Lee, C., & Yang, M. (2018). Influence of enlarged section parameters on pressure transients of high-speed train passing through a tunnel. *Journal of Central South University, 25*(11), 2831–2840. https://doi.org/10.1007/s11771-018-3956-8

Xiang, X., Xue, L., Wang, B., & Zou, W. (2018). Mechanism and capability of ventilation openings for alleviating micro-pressure waves emitted from high-speed railway tunnels. *Building and Environment, 132*, 245–254. https://doi.org/10.1016/j.buildenv.2018.01.045

Xiong, X., Zhu, L., Zhang, J., Li, A., Li, X., & Tang, M. (2020). Field measurements of the interior and exterior aerodynamic pressure induced by a metro train passing through a tunnel. *Sustainable Cities and Society, 53*, Article 101928. https://doi.org/10.1016/j.scs.2019.101928

Xue, Z., Han, B., Zhang, H., Xin, D., Zhan, J., & Wang, R. (2021). External suction-blowing method for controlling vortex-induced vibration of a bridge. *Journal of Wind Engineering and Industrial Aerodynamics, 215*, Article 104661. https://doi.org/10.1016/j.jweia.2021.104661

Yang, X., Shou, A., Zhang, R., Quan, J., Li, X., & Niu, J. (2021). Numerical study on transient aerodynamic behaviors in a subway tunnel caused by a metro train running between adjacent platforms. *Tunnelling and Underground Space Technology, 117*, Article 104152. https://doi.org/10.1016/j.jweia.2021.104661

Yu, S., Liu, G., & Yin, C. (2021). Understanding spatial-temporal travel demand of free-floating bike sharing connecting with metro stations. *Sustainable Cities and Society, 74*, Article 103162. https://doi.org/10.1016/j.scs.2021.103162

Zailani, M. A. H., Sabudin, R., Rahman, R. A., Saiboon, I. M., Ismail, A., & Mahdy, Z. A. (2020). Drone for medical products transportation in maternal healthcare: A systematic review and framework for future research. *Medicine, 99*(36), e21967. https://doi.org/10.1097/md.0000000000021967

Zhang, L., Liu, H., Stoll, N., & Thurow, K. (2017). Influence of tunnel aerodynamic effects by slope of equal-transect ring oblique tunnel portal. *Journal of Wind Engineering and Industrial Aerodynamics, 169*, 106–116. https://doi.org/10.1016/j.jweia.2017.07.011

Zhang, L., Thurow, K., Stoll, N., & Liu, H. (2018). Influence of the geometry of equal-transect oblique tunnel portal on compression wave and micro-pressure wave generated by high-speed trains entering tunnels. *Journal of Wind Engineering and Industrial Aerodynamics, 178*, 1–17. https://doi.org/10.1016/j.jweia.2018.05.003

Zhang, Y., & Li, X. (2021). Numerical analysis on the condenser inlet air temperature of train-mounted air conditioner when a train stops in subway station tunnel. *Sustainable Cities and Society, 69*, Article 102793. https://doi.org/10.1016/j.scs.2021.102793

Zhong, S., Qian, B., Yang, M., Wu, F., Wang, T., Tan, C., & Ma, J. (2021). Investigation on flow field structure and aerodynamic load in vacuum tube transportation system. *Journal of Wind Engineering and Industrial Aerodynamics, 215*, Article 104681. https://doi.org/10.1016/j.jweia.2021.104681

Zhou, D., Wu, L., Tan, C., & Hu, T.e. (2021). Study on the effect of dimple position on drag reduction of high-speed maglev train. *Transportation Safety and Environment, 3*(4), tdab027. https://doi.org/10.1093/tse/tdab027

Zhou, M., Liu, T., Xia, Y., Li, W., & Chen, Z. (2022). Comparative investigations of pressure waves induced by trains passing through a tunnel with different speed modes. *Journal of Central South University, 29*(8), 2639–2653. https://doi.org/10.1007/s11771-022-5098-2